RADIATIVE MAGNETIC RECONNECTION NEAR ACCRETING BLACK HOLES

Andrei M. Beloborodov
Physics Department and Columbia Astrophysics Laboratory, Columbia University, 538 West 120th Street New York, NY 10027;
amb@phys.columbia.edu
Draft version January 12, 2017

ABSTRACT

A radiative mechanism is proposed for magnetic flares near luminous accreting black holes. It is based on recent first-principle simulations of magnetic reconnection, which show a hierarchical chain of fast-moving plasmoids. The reconnection occurs in a compact region (comparable to the black hole radius), and the chain experiences fast Compton cooling accompanied by electron-positron pair creation. The distribution of plasmoid speeds is shaped by radiative losses, and the self-regulated chain radiates its energy in hard X-rays. The mechanism is illustrated by Monte-Carlo simulations of the transfer of seed soft photons through the reconnection layer. The emerging radiation spectrum has a cutoff near 100 keV similar to the hard-state spectra of X-ray binaries and AGN. We discuss how the chain cooling differs from previous phenomenological emission models, and suggest that it can explain the hard X-ray activity of accreting black holes from first principles. Particles accelerated at the X-points of the chain produce an additional high-energy component, explaining "hybrid Comptonization" observed in Cyg X-1.

Subject headings: accretion, accretion disks — magnetic reconnection — radiation mechanisms: general — relativistic processes — stars: black holes — galaxies: active

1. INTRODUCTION

Accretion disks around black holes are bright sources of X-rays. They are observed to radiate in "soft" and "hard" states (e.g. Zdziarski & Gierliński 2004). The soft state is dominated by quasi-thermal emission from an optically thick accretion disk, and the hard state is dominated by hard X-rays that come from a plasma of a moderate optical depth. A canonical example is Cyg X-1. Its hard-state spectrum is usually explained by a phenomenological model of Comptonization of soft X-rays in a hot plasma ("corona") with electron temperature $kT_e \sim 100$ keV. The weak MeV tail of the observed spectrum is explained by the presence of additional nonthermal electrons (Coppi 1999; McConnell et al. 2002).

This phenomenological model invokes an unspecified heating mechanism that balances the fast Compton cooling. The thermal electrons are cooled by seed soft photons through unsaturated Comptonization (e.g. Rybicki & Lightman 1979), which satisfies the condition

$$y \sim 4 \frac{kT_e}{m_e c^2} \tau_{\rm T}^2 \sim 1, \qquad (1)$$

where $\tau_{\rm T} \gtrsim 1$ is the (Thomson) scattering optical depth of the heated plasma, and $m_e c^2 = 511$ keV is the electron rest-mass energy. This condition, together with $kT_e \sim 100$ keV, implies $\tau_{\rm T} \sim 1$. Similar temperatures and optical depths are also inferred from observations of AGN (Fabian et al. 2015).

Why the heated plasma has the optical depth $\tau_{\rm T} \sim 1$ is still an open issue. One possibility is that $\tau_{\rm T}$ is regulated by creation of $e^{\pm}$ pairs in photon-photon collisions (Guilbert et al. 1983; Svensson 1987; Stern et al. 1995). A remarkable feature of observed spectra is the sharpness of the cutoff near 100 keV; in particular, the hard-state luminosity of Cyg X-1 drops by a factor ~ 30 between 200 keV and 1 MeV. This is often interpreted as evidence

for Comptonization by nearly isothermal plasma, with an exponentially suppressed electron population at energies $E_e \gg kT_e \approx 100$ keV. It is, however, unclear why the emission region is nearly isothermal, as T_e must reflect the heating rate, which varies in space and time.

Attempts to develop an emission model from first principles, avoiding phenomenological assumptions, must be based on a concrete mechanism of energy release. A plausible mechanism is magnetic reconnection (Galeev et al. 1979). It occurs in current sheets formed by magnetic loops above the accretion disk, resembling solar activity. Unlike solar flares, the current sheets are generated mainly by the disk rotation. Differential rotation of the magnetic loop footpoints (one of which may be on the black hole) leads to inflation and opening of the loop, with a current sheet separating the two opposite open magnetic fluxes (Romanova et al. 1998; Parfrey et al. 2015). The energy of the inflated loop is then released through reconnection of the two fluxes. Another difference from solar flares is that the magnetic energy density in the disk corona, $B^2/8\pi$, can strongly dominate over the rest-mass density of the plasma, ρc^2, i.e. reconnection is relativistic.

A number of ab initio microscopic simulations of relativistic magnetic reconnection have been performed using particle-in-cell (PIC) method (Sironi & Spitkovsky 2014; Melzani et al. 2014; Guo et al. 2016; Sironi et al. 2016; Werner et al. 2016). The simulations demonstrate a chain of distinct plasmoids in the reconnection layer, carrying a broad nonthermal electron distribution rather than a Maxwellian plasma. The results have been applied to nonthermal emission from relativistic outflows, including gamma-ray flares in the Crab nebula and blazars (Cerutti et al. 2014; Kagan et al. 2016; Petropoulou et al. 2016).

The PIC simulations have not explored yet the regime of dominant radiative losses that become inevitable if

magnetic reconnection occurs in a compact region near a luminous accreting black hole. In this paper, we make analytical estimates of radiative losses and their effects on the plasmoid chain. In particular, inverse Compton scattering and $e^{\pm}$ pair creation play a key role. Then we use a Monte-Carlo simulation to evaluate the Comptonized radiation spectrum produced by a compact magnetic flare with a relativistic plasmoid chain. The results appear consistent with the observed hard-state spectra of accreting black holes, offering a solution to the puzzle of the 100-keV cutoff.

2. BASIC PARAMETERS

2.1. *Magnetization σ and compactness ℓ*

One dimensionless parameter of the reconnection problem is the magnetization,

$$\sigma = \frac{B^2}{4\pi\rho c^2} = \frac{2U_B}{\rho c^2}, \qquad (2)$$

where B is the magnetic field, $U_B = B^2/8\pi$, and ρ is the mass density of the plasma. We will neglect the guide field, i.e. assume that $\mathbf{B}$ reverses direction across the current sheet. We also assume that the plasma before reconnection is cool (without energy dissipation, the coronal plasma is kept at the Compton temperature of the local radiation field, $kT_C \ll m_e c^2$). Reconnection in a magnetically dominated corona, $\sigma > 1$, is of main interest for this paper. Then fast magnetosonic waves have the Lorentz factor $\gamma \approx \sigma^{1/2}$, and the plasma bulk motions in the reconnection layer achieve a similar $\gamma \sim \sigma^{1/2}$ (Lyubarsky 2005; Sironi et al. 2016). The parameter σ also controls the energy release per particle in the flare.

In the presence of radiative losses, a second dimensionless parameter appears in the reconnection problem — the "compactness parameter" ℓ, which determines how the timescale for electron radiative cooling compares with the light crossing time of the current sheet, s/c. In particular, the timescales for inverse Compton cooling (with Thomson scattering) and synchrotron cooling are given by

$$\frac{t_{IC}}{s/c} = \frac{3}{4\gamma_e\,\ell_{rad}}, \qquad \frac{t_{syn}}{s/c} = \frac{3}{4\gamma_e\,\ell_B \sin^2\theta}, \qquad (3)$$

where $\gamma_e \gg 1$ is the electron Lorentz factor, θ is the electron pitch angle relative to the magnetic field, s is the size of the current sheet, and

$$\ell_{rad} = \frac{U_{rad}\sigma_T s}{m_e c^2}, \qquad \ell_B = \frac{U_B \sigma_T s}{m_e c^2}. \qquad (4)$$

Here m_e is the electron mass and σ_T is the Thomson cross section. In the radiative regime, most of the dissipated magnetic energy is immediately converted to radiation, which escapes with speed $\sim c$, as long as the optical depth of the flare region is not much larger than unity. Then $U_{rad}c \sim U_B v_{rec}$ and

$$\ell_{rad} \sim \frac{v_{rec}}{c}\,\ell_B, \qquad (5)$$

where $v_{rec} \sim 0.1c$ is the reconnection speed (Lyubarsky 2005).

Radiation receives energy from the reconnection layer through Compton scattering. Let U_s be the density of soft ("seed") radiation in the reconnection region, and

$$\ell_s = \frac{U_s \sigma_T s}{m_e c^2}. \qquad (6)$$

The ratio $U_{rad}/U_s = \ell_{rad}/\ell_s$ controls the hardness of the Comptonized spectrum emerging from the reconnection layer. U_s may be supplied externally, in particular by radiation from a dense, cool accretion disk. It may also be created locally by the dissipation process itself, due to synchrotron emission from electrons accelerated in the magnetic flare.

2.2. *Magnetic flares near black holes*

It is straightforward to estimate the characteristic ℓ_B for a current sheet created near a black hole of mass M accreting with rate $\dot{M}$. The energy density of the coronal magnetic field rooted in the accretion disk, U_B, is a fraction of the disk pressure P. It is related to the viscous stress driving accretion, $\alpha P \approx \dot{M}(GMr)^{1/2}/4\pi r^2 H$, where $\alpha = 0.01 - 0.1$ is the Shakura-Sunyaev viscosity parameter, and H is the half-thickness of the disk at a radius r. A conservative estimate for U_B is given by

$$U_B \sim \frac{\dot{M}(GMr)^{1/2}}{4\pi r^2 H}. \qquad (7)$$

The characteristic radius of the most luminous region is small — comparable to $r_g = 2GM/c^2$ — in particular if the black hole is rapidly rotating.

An accreting black hole with luminosity L has the accretion rate $\dot{M} = L/\varepsilon c^2$, where $\varepsilon \sim 0.1$ is the radiative efficiency. A luminous accreting black hole typically has L varying around $0.1L_{Edd}$ where $L_{Edd} = 4\pi GMm_p c/\sigma_T$ is the Eddington limit, and the scale-height of its accretion disk is $H \lesssim r_g$. This gives a rough estimate for U_B and the corresponding compactness parameter of a current sheet of size $s \sim r_g$,

$$U_B \sim \frac{m_p c^2}{\sigma_T r_g}, \qquad \ell_B \sim \frac{m_p}{m_e}. \qquad (8)$$

Stronger fields may be sustained in the model of magnetically arrested disks (Tchekhovskoy et al. 2011). A typical expected value for ℓ_B in bright X-ray binaries or AGN is between 10^3 and 10^4.

Equation (5) gives the corresponding $\ell_{rad} \sim 0.1\ell_B \sim 10^2 - 10^3$. It is greater than the average compactness $\bar{\ell}_{rad} = F\sigma_T r/m_e c^3$, where F is the average radiation flux in the vicinity of the black hole. For instance, the luminosity of Cyg X-1 in the hard state, $L \sim 3\times 10^{37}$ erg s^{-1}, corresponds to $\bar{\ell}_{rad} \sim 10$ (assuming that the luminosity emerges from a few Schwarzschild radii r_g). The coronal activity should occur in flares, i.e. the emission is localized in space and time, and the flares have the compactness parameter $\ell_{rad} \gg \bar{\ell}_{rad}$. Millisecond flares with luminosities increased by a factor ~ 20 above the average emission have been detected in Cyg X-1 (Gierliński & Zdziarski 2003).

The estimate (8) gives a characteristic magnetic field,

$$B = (8\pi U_B)^{1/2} \sim 10^8 \left(\frac{M}{10M_\odot}\right)^{-1/2} \text{ G.} \qquad (9)$$

The corresponding timescale for electron gyration, $\omega_B^{-1} = m_e c/eB$, is many orders of magnitude shorter

than the light-crossing time of the region,

$$\frac{c}{\omega_B r_g} \sim 10^{-11} \left(\frac{M}{10M_\odot}\right)^{-1/2}. \qquad (10)$$

The length c/ω_B is the smallest scale in the reconnection problem. The corresponding ion scale in an electron-proton plasma, $c/\omega_B = m_p c^2/eB$, is larger by the factor of m_p/m_e, but still much smaller than r_g.

2.3. Pair creation and optical depth

The reconnection layer has the characteristic thickness $h \sim \beta_{\rm rec}s$ (where $\beta_{\rm rec} = v_{\rm rec}/c$), and its optical depth is defined by

$$\tau_{\rm T} = n_e \sigma_{\rm T} h, \qquad (11)$$

where n_e is the number density of electrons or positrons. Without $e^\pm$ plasma, the electron density n_e equals the proton density n_p. The optical depth of the electron-proton plasma in a flare with compactness ℓ_B and magnetization σ may be expressed as

$$\tau_{\rm T}^{ep} \sim \frac{2\beta_{\rm rec}}{\sigma}\frac{\ell_B}{m_p/m_e} \ll 1. \qquad (12)$$

Pair creation is inevitable as soon as the flare spectrum extends above $m_e c^2 = 0.511$ MeV, because the MeV photons convert to $e^\pm$ pairs through photon-photon (γ-γ) collisions (Guilbert et al. 1983). The absorption optical depth $\tau_{\gamma\gamma}$ seen by a gamma-ray depends on its energy $E = \epsilon m_e c^2$. Photons with $\epsilon \gg 1$ mainly interact with target photons of low energies $\epsilon_t \sim \epsilon^{-1}$ (near the threshold of γ-γ reaction). Photons of energies just above $\epsilon \sim 1$ interact with each other, with a cross section $\sigma_{\gamma\gamma} \sim 0.1\sigma_{\rm T}$. It is convenient to define

$$\ell_1 = \frac{U_1 \sigma_{\rm T} s}{m_e c^2} = \frac{U_1}{U_B}\ell_B, \qquad (13)$$

where U_1 is the energy density of photons with $\epsilon \sim 1$. Only a small fraction $\sim 10^{-2}$ of Cyg X-1 luminosity is observed in the MeV band, which suggests $\ell_1 \sim 10^{-2}\ell_{\rm rad} \sim 2 - 10$.

Most of the pairs are created inside or near the reconnection layer. The rate of photon-photon collisions is quickly reduced with distance z from the MeV source due to reduced angles between the colliding photons (Beloborodov 1999b). In addition, the MeV emission is beamed along the reconnection layer, as will be discussed below. The characteristic thickness of the pair-production region, $z/s \sim 0.2$, is comparable to the thickness of the reconnection layer $h/s \sim v_{\rm rec}/c$.

The rate of pair creation by the MeV photons is given by

$$\dot{n}_+ \sim \sigma_{\gamma\gamma}c n_1^2, \qquad \sigma_{\gamma\gamma} = \eta\sigma_{\rm T}, \qquad n_1 \sim \frac{U_1}{m_e c^2}, \quad (14)$$

where $\eta \sim 0.1$ (Svensson 1987). The residence time of plasma in the reconnection layer is

$$t_{\rm res} \sim \frac{h}{v_{\rm rec}} \sim \frac{s}{c}, \qquad (15)$$

and the density of positrons accumulated in the plasma before it is ejected from the flare is

$$n_+ \sim \dot{n}_+ t_{\rm res} \sim \eta\sigma_{\rm T}n_1^2 s. \qquad (16)$$

This is a valid estimate for n_+ if the annihilation of $e^\pm$ pairs is negligible, i.e. if the annihilation timescale $t_{\rm ann} > t_{\rm res}$. In the opposite case, n_+ is determined by the annihilation balance,

$$\dot{n}_{\rm ann} = \frac{3}{8}\sigma_{\rm T}c\, n_+ n_- \sim \sigma_{\gamma\gamma}c\, n_1^2. \qquad (17)$$

Then, using $n_- \approx n_+$, one finds $n_+ \sim (8\eta/3)^{1/2}n_1$. Note that $t_{\rm ann} = n_+/\dot{n}_{\rm ann} = 8/3\sigma_{\rm T}c\, n_+$, and the boundary between the two cases, $t_{\rm ann} = t_{\rm res}$, occurs when $\ell_1 \approx \ell_\star = (8/3\eta)^{1/2} \approx 5$.

The optical depth of $e^\pm$ pairs of density $n_\pm = 2n_+$ is given by

$$\tau_{\rm T} \sim n_\pm \sigma_{\rm T} h \sim \frac{16}{3}\beta_{\rm rec} \times \begin{cases} (\ell_1/\ell_\star)^2, & \ell_1 < \ell_\star \\ \ell_1/\ell_\star, & \ell_1 > \ell_\star \end{cases} \quad (18)$$

The characteristic optical depth $\tau_{\rm T} \sim (16/3)\beta_{\rm rec}$ is close to unity. The expected ℓ_1 is comparable to $\ell_\star$ and is unlikely to greatly exceed it; hence $\tau_{\rm T} \gg 1$ is not expected.

An estimate for pair density may also be formulated assuming that a fraction $f_{\rm HE}$ of the magnetic energy supplied to the reconnection layer converts to high-energy particles. The particles will produce inverse Compton (IC) emission, in particular if their synchrotron losses are suppressed by small pitch angles or by synchrotron self-absorption. Practically all emission above a few MeV is blocked by the γ-γ reaction and reprocessed to lower energies through creation of secondary pairs. As a result, a fraction $Y \ll 1$ of the injected particle energy converts to the rest-mass of the secondary $e^\pm$ pairs (Svensson 1987). If synchrotron losses are negligible then $Y \sim 0.1$. The reduction of Y due to synchrotron losses depends on the injection energy of the accelerated particles, which will be discussed below.

The resulting pair creation rate in the reconnection layer is

$$\dot{n}_\pm \sim \frac{Y f_{\rm HE} U_B}{t_{\rm res} m_e c^2}. \qquad (19)$$

The annihilation balance is approached if $Y f_{\rm HE}\ell_B > 16/3$. Defining $u = (3/16)Y f_{\rm HE}\ell_B$, one can express the optical depth of the pair-loaded reconnection layer as

$$\tau_{\rm T} \sim \frac{16}{3}\beta_{\rm rec} \times \begin{cases} u, & u < 1 \\ u^{1/2}, & u > 1 \end{cases} \qquad (20)$$

3. RADIATIVE PLASMOID CHAIN

The magnetic flare develops as the current sheet separating two opposite magnetic fluxes becomes tearing-unstable, which leads to the formation of a chain of plasmoids separated by "X-points" of the magnetic field lines (Uzdensky et al. 2010). The X-points and plasmoids are continually created with sizes comparable to the Larmor radius of the heated particles, $w_{\rm min} \sim r_{\rm L} \sim \sigma c/\omega_B$. The plasmoids merge and grow in size, forming a hierarchical chain (Figure 1). The maximum plasmoid width, $w_{\rm max}$, is a significant fraction of the size of the reconnection layer (Loureiro et al. 2012; Sironi et al. 2016). "Monster" plasmoids can grow up to a significant fraction of r_g, and so a huge range of scales exists in the plasmoid chain, from $r_{\rm L}$ to r_g.
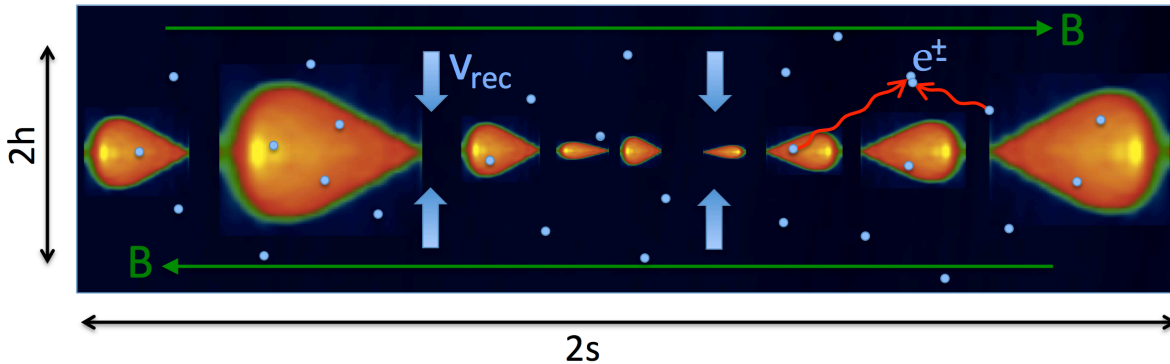
FIG. 1.— Schematic picture of the reconnection layer. Opposite magnetic fluxes converge toward the midplane of the layer with velocity $v_{\rm rec} \sim 0.1c$. The reconnected magnetic field forms closed islands (plasmoids), which move horizontally with various relativistic speeds. Their Lorentz factors γ reach $\sigma^{1/2}$ where σ is the magnetization parameter defined in Equation (2). The Lorentz factors are controlled by radiative losses and related to the plasmoid size w as discussed in Section 3.3. The plasmoids have a broad distribution of w and γ, and form a self-similar chain. They radiate hard X-rays with a spectrum calculated in Section 4. Photons with energies $E > m_e c^2$ convert to $e^{\pm}$ pairs in photon-photon collisions (shown by the red arrows); this process greatly increases the optical depth of the reconnection layer.

3.1. Energy deposition

The PIC simulations show that about half of the magnetic energy advected into the reconnection layer is dissipated. The dissipation occurs in two ways:
(1) A fraction of particles are accelerated by the strong electric fields $E \sim B$ near the X-points. The energy gain E_e has the characteristic value of $\sim (\sigma/2)mc^2$, comparable to the average energy released per particle in the magnetic flare ($m = m_e$ for pair plasma and $m = m_p/2$ for hydrogen).
(2) The plasmoids are accelerated by magnetic stresses to high Lorentz factors (up to $\gamma = \sigma^{1/2}$), collide, and merge, dissipating part of their energy.

Recent PIC simulations with large computational boxes show that most of the dissipation is associated with hierarchical mergers rather than X-points (Sironi et al. 2016). As reconnection develops and $w_{\rm max}$ grows, the role of particle acceleration at the X-points is limited to an initial energy boost of fresh particles, which is followed by energy gains in the mergers.

Simulations of reconnection in a plasma composed of electrons, protons, and $e^{\pm}$ pairs have not been performed yet. Let

$$Z = 1 + \frac{n_{\pm}}{n_p} \qquad (21)$$

be the "pair loading factor," where n_p and $n_{\pm}$ are the number densities of protons and pairs, respectively. In an extended range of $1 < Z < m_p/m_e$ the plasma rest mass is dominated by ions while the particle number is dominated by $e^{\pm}$ pairs. Without radiative losses, the behavior of a particle in relativistic magnetic reconnection ($\sigma \gg 1$) is controlled by its charge and should be independent of its mass. In particular, the energy gain at an X-point, the corresponding Larmor radius, and the subsequent energy gains in mergers must be the same for protons and $e^{\pm}$, as indeed observed in electron-ion PIC simulations (Melzani et al. 2014)).

Flares in the magnetically dominated corona, $\sigma \gg 1$, have $\tau_{\rm T}^{ep} \ll 1$ (Equation 12) and develop $\tau_{\rm T} \sim 1$ due to copious pair creation, which implies $Z \gg 1$. It is useful to express σ in the form,

$$\sigma = \frac{2U_B}{n_{\pm} m_e c^2 + n_p m_p c^2} = \sigma_0 \left(1 + \frac{n_p m_p}{n_{\pm} m_e}\right)^{-1}, \qquad (22)$$

where

$$\sigma_0 = \frac{2U_B}{n_{\pm} m_e c^2} = \frac{2\beta_{\rm rec} \ell_B}{\tau_{\rm T}}, \qquad \tau_{\rm T} \approx n_{\pm} \sigma_{\rm T} h. \qquad (23)$$

Assuming that reconnection dissipates about half of the magnetic energy, as observed in the PIC simulations, the average energy released per particle in a plasma with $Z \gg 1$ is $U_B/2n_{\pm}$. This gives the average electron/positron Lorentz factor,

$$\bar{\gamma}_e \approx \frac{\sigma_0}{4} \approx \frac{\beta_{\rm rec} \ell_B}{2\tau_{\rm T}}. \qquad (24)$$

Substituting $\beta_{\rm rec} \sim 0.1$, $\ell_B \sim m_p/m_e$, and $\tau_{\rm T} \sim 1$, one finds $\bar{\gamma}_e \sim 10^2$. This is also the expected characteristic Lorentz factor acquired by particles at the X-points.

Energy is also deposited in the chain through plasmoid acceleration by magnetic stresses. We now estimate how this energy deposition is distributed between plasmoids of different sizes w. In a self-similar chain, the distribution of plasmoid number N over w follows a power law,

$$\frac{dN}{d\ln w} \propto w^{-q}. \qquad (25)$$

Here N is counted in a two-dimensional cross section of the reconnection region (in the reconnection plane xz). A simplified chain model of Uzdensky et al. (2010) give $q = 1$, and more detailed considerations suggest $q \approx 0$ (Huang & Bhattacharjee 2012). Numerical simulations by Sironi et al. (2016) show that q is close to zero on scales $w \ll w_{\rm max}$ (the self-similar chain) and increases as w approaches $w_{\rm max}$.

The plasmoids are pushed and accelerated by the gradients of magnetic stresses. Using the plasmoid size w as a characteristic scale to estimate the gradient, one may write the pushing force (per unit volume) in the form

$$f_{\rm push} = \xi \frac{U_B}{w}. \qquad (26)$$

The dimensionless coefficient $\xi < 1$ may be found from numerical simulations. The simulations show that plasmoids accelerate significantly slower than their light-crossing time w/c, which implies $\xi \ll 1$. Sironi et al. (2016) find $\xi \sim \beta\,\beta_{\rm rec}$ where $\beta = v/c$ is the plasmoid speed. This estimate may change when the chain experiences strong Compton drag, and this needs to be explored with new PIC simulations. Note also that large fluctuations in plasmoid motions indicate that ξ has a rather broad distribution around its mean value. However, below we only consider the simplest model with a fixed ξ.

The work done by $f_{\rm push}$ (integrated over the plasmoid cross section in the reconnection plane) scales as $w^2 f_{\rm push} v$. This can be used to estimate the scaling law for the energy deposition into the plasmoid bulk motions in the self-similar chain. The deposited power L is distributed over w as

$$\frac{dL}{d\ln w} \propto w^2 f_{\rm push}\, v\, \frac{dN}{d\ln w} \propto \xi\, w^{1-q}\,\beta, \qquad (27)$$

where $\beta \approx 1$ for relativistic plasmoids. This rough estimate may be refined by direct measurements of $dL/d\ln w$ in PIC simulations. For the radiative chain model described below (Section 3.3) it is important that the power deposited into bulk motions is broadly distributed over plasmoid size w and, for relativistic plasmoids, $dL/d\ln w$ decreases toward small w.

3.2. Cooling of young hot plasmoids

Electrons and positrons accelerated at the X-points gain Lorentz factors comparable to $\bar{\gamma}_e$ on the timescale,

$$t_X \sim \frac{\bar{\gamma}_e m_e c}{eB} \sim 10^{-9} \left(\frac{M}{10 M_\odot}\right)^{-1/2} \frac{r_g}{c}. \qquad (28)$$

The shortest possible timescale for cooling is given by

$$t_{\rm syn}^{\rm min} \sim \frac{m_e c}{\sigma_{\rm T} U_B \bar{\gamma}_e} \sim 10^{-5} \frac{r_g}{c}, \qquad (29)$$

where we substituted $\bar{\gamma}_e$ from Equation (24) and U_B from Equation (8). One can see that $t_{\rm syn} \gg t_X$, so the accelerated particles are pushed into young small plasmoids before they have a chance to radiate their energy.

The cooling time is also longer than the time it takes a nascent plasmoid to develop a bulk Lorentz factor $\gamma \gg 1$. Then the Lorentz factor of an electron/positron in the lab frame may be written as

$$\gamma_e \sim \gamma \gamma_e', \qquad (30)$$

where γ_e' is a "thermal" Lorentz factor measured in the plasmoid rest frame. Synchrotron losses can reduce only γ_e' and occur slower if $\gamma \gg 1$. The cooling time in the plasmoid frame $t_{\rm syn}' \propto (B'^2 \gamma_e')^{-1}$, and the cooling time in the static lab frame is $t_{\rm syn} = \gamma t_{\rm syn}'$. Synchrotron self-absorption strongly suppresses cooling when $\gamma_e' \lesssim 10$.

The timescale for IC cooling in the plasmoid rest frame is given by

$$t_{\rm IC}' \sim \frac{m_e c}{\sigma_{\rm T} \zeta_{\rm KN} \gamma^2 U_{\rm rad} \gamma_e'}, \qquad (31)$$

where we used $U_{\rm rad}' \sim \gamma^2 U_{\rm rad}$, and $\zeta_{\rm KN} < 1$ describes the reduction due to Klein-Nishina corrections. An upper

bound on $t_{\rm IC}'$ may be estimated as $t_{\rm IC}' \lesssim m_e c / \sigma_{\rm T} U_{\rm rad}$, which gives

$$t_{\rm IC}' \lesssim \frac{10}{\ell_B} \frac{r_g}{c}. \qquad (32)$$

The maximum cooling time should be compared with the typical age of plasmoids of size w: $t_{\rm age}' \sim 10(w/c)$ (Sironi et al. 2016). This comparison shows that plasmoids of sizes $w \gg r_g/\ell_B$ must be cooled to a non-relativistic temperature. The $e^\pm$ pairs trapped in large plasmoids tend to Compton equilibrium with radiation, which corresponds to a temperature $kT_{\rm C} \ll m_e c^2$. Only the ion component can keep the heat received in reconnection.

This conclusion is not changed by heating due to mergers, as the mergers of large plasmoids occur slower than their cooling. In the heating picture discussed by Sironi et al. (2016), the energies gained by the plasmoid particles should be proportional to their energies before the merger, similar to simple adiabatic heating. Then the hot ions are strongly heated while the cooled electrons receive much less energy.

Since the plasma is dominated by $e^\pm$ pairs ($Z \gg 1$), their cooling implies losing most of the plasma enthalpy. As a result, the inertial mass of the plasma is reduced. However, the plasmoid does not become much lighter after cooling, because a large fraction of its effective mass density is carried by the magnetic field, $\rho_{\rm eff} \approx B^2/4\pi c^2$. The strong cooling only implies that the plasmoids assume a nearly force-free configuration. The force-free hierarchical chains are observed in simulations of reconnection that neglect the plasma inertia (Parfrey et al. 2013, 2015). They show the same X-points, mergers, and the growth of monster plasmoids. The dynamics of force-free plasmoids are fully controlled by the magnetic stresses in the chain, which are not much different from those in the PIC models without cooling.

3.3. Compton drag on large plasmoids

The plasmoid chain has a regular motion component toward the exit from the reconnection layer and comparable or faster random motions. Scattering of ambient photons creates effective viscosity for plasmoids.[1] As long as scattering occurs in Thomson regime, the drag force per unit volume applied to an optically thin plasmoid moving through radiation of density $U_{\rm rad}$ is given by

$$f_{\rm drag} \approx \beta \gamma^2 \gamma_e'^2 U_{\rm rad} \sigma_{\rm T}\, n_\pm, \qquad (33)$$

where $\gamma = (1 - \beta^2)^{-1/2}$ is the bulk Lorentz factor, and γ_e' is the random ("thermal") Lorentz factor of electrons (or positrons) in the plasmoid rest frame; $\gamma_e \approx \gamma \gamma_e'$ is the characteristic electron Lorentz factor in the lab frame. The plasmoid momentum per unit volume is $\sim \beta B^2/4\pi c$,

---

[1] Unlike synchrotron radiation, the IC photons with energies $E_{\rm IC}'$ in the plasmoid rest frame have a significant average momentum $\sim E_{\rm IC}'/c$, even when the energetic electrons are isotropic in this frame. The asymmetry of IC radiation is related to the fact that the target soft radiation is beamed in the plasmoid frame due to relativistic aberration. Scattering by electrons moving against the beam is more frequent, leading to preferential IC emission against the beam direction (Odell 1981; Phinney 1982; Sikora et al. 1996). The bias in the scattering direction causes the plasmoid deceleration.

and the plasmoid deceleration timescale is

$$t_{\rm drag} \sim \frac{\beta B^2}{4\pi c f_{\rm drag}} \sim \frac{U_B}{U_{\rm rad}} \frac{1}{\gamma^2 \gamma_e'^2 \sigma_{\rm T} n_\pm c}. \qquad (34)$$

Note that $t_{\rm drag}$ is related to the Compton cooling time $t_{\rm IC}$ by

$$\frac{t_{\rm drag}}{t_{\rm IC}} \sim \frac{U_B}{U_{\rm kin}}, \qquad U_{\rm kin} = \gamma_e m_e c^2 n_\pm. \qquad (35)$$

In a radiative plasmoid chain, $U_{\rm kin} \ll U_B$ and hence $t_{\rm drag} \gg t_{\rm IC}$, so the plasmoids are strongly cooled before deceleration. In the strong cooling limit, $\gamma_e' \approx 1$, $\gamma_e \approx \gamma$, and the drag force is $f_{\rm drag} \approx \beta\gamma^2 U_{\rm rad}\sigma_{\rm T} n_\pm$.

The plasmoids are pushed by magnetic forces $f_{\rm push} = \xi U_B/w$ (Section 3.1) and capable of accelerating as long as $f_{\rm drag} < f_{\rm push}$. The ratio of the two forces may be written as

$$\frac{f_{\rm drag}}{f_{\rm push}} = \beta\gamma^2 \frac{\tau_{\rm pl}}{\tau_\star}, \qquad \tau_\star \equiv \xi \frac{U_B}{U_{\rm rad}} \approx \frac{\xi}{\beta_{\rm rec}}. \qquad (36)$$

Here $\tau_{\rm pl}$ is the optical depth of the plasmoid of width w,

$$\tau_{\rm pl} = n_\pm \sigma_{\rm T} w. \qquad (37)$$

The drag is not important if $f_{\rm drag}/f_{\rm push} < 1$, and from Equation (36) one concludes that plasmoids with $\tau_{\rm pl} < \tau_\star$ can become relativistic, $\beta\gamma^2 > 1$. The drag limits their Lorentz factors to $\gamma \approx (\tau_\star/\tau_{\rm pl})^{1/2}$. Plasmoids with $\tau_{\rm pl} < \tau_\star/\sigma$ are limited by the "ceiling" $\gamma \leq \sigma^{1/2}$, which is not related to drag and observed in the PIC simulations without radiative losses (Sironi et al. 2016).

Monster plasmoids have sizes comparable to the thickness of the reconnection layer h, and their optical depths are $\tau_{\rm pl} \sim \tau_{\rm T}$. If $\tau_{\rm T} > \tau_\star$ (expected for $\xi \ll 1$, see Section 3.1) then the drag limits the plasmoid speeds even in the nonrelativistic regime $\beta\gamma < 1$. Note also that even without Compton drag, the largest plasmoids in the chain are pushed only to mildly relativistic speeds $v \sim 0.5c$ (Sironi et al. 2016).

The bulk motion is saturated, $f_{\rm drag} \approx f_{\rm push}$, if the duration of the magnetic force, $t_{\rm push}$, exceeds $t_{\rm drag}$. In the simplest model, $t_{\rm push}$ is the residence time in the chain, $t_{\rm res} \approx s/\beta c$. Using $U_{\rm rad}/U_B \approx \beta_{\rm rec} \approx h/s$, the ratio $t_{\rm drag}/t_{\rm res}$ is conveniently expressed as

$$\frac{t_{\rm drag}}{t_{\rm res}} \sim \frac{\beta}{\gamma^2 \tau_{\rm T}}, \qquad \tau_{\rm T} = n_\pm \sigma_{\rm T} h. \qquad (38)$$

One can see that $t_{\rm drag} < t_{\rm res}$ for all plasmoids as long as the reconnection layer has a substantial optical depth $\tau_{\rm T} \gtrsim 1$. However, in a realistic chain $f_{\rm push}$ varies stochastically on timescales $t_{\rm push} \ll t_{\rm res}$. Therefore, deviations from the force balance are expected, and the condition $f_{\rm drag} \leq f_{\rm push}$ only defines an upper limit for the plasmoid speed.

This upper limit still represents a characteristic speed of plasmoids of a given optical depth $\tau_{\rm pl}$,

$$\beta\gamma^2 \approx \frac{\tau_\star}{\tau_{\rm pl}}. \qquad (39)$$

It can also be expressed using an effective y-parameter — the product of the scattering probability $\tau_{\rm pl}$ (for a soft photon propagating through the plasmoid) and the average energy gain in scattering $\Delta E/E \sim \beta^2\gamma^2$,

$$y_{\rm pl} = a\tau_{\rm pl}, \qquad a \equiv \beta^2\gamma^2. \qquad (40)$$

The parameter $y_{\rm pl}$ is the amplification factor of radiation flowing through the plasmoid. Equation (39), which corresponds to $f_{\rm drag} = f_{\rm push}$, can be stated as an energy balance condition: the work done by magnetic forces, $\dot{U} = f_{\rm push}v$, converts to radiation energy that escapes the plasmoid on the timescale $t_{\rm esc} \sim w/c$: $\dot{U} = y_{\rm pl}U/t_{\rm esc}$.

Equation (27) described how the power L deposited in the chain is distributed over the plasmoid size w. For calculations of photon Comptonization it is important to know how the power is distributed over the parameter $a = \beta^2\gamma^2$, which controls the photon energy gain per scattering. We will roughly estimate this distribution using Equation (39) and considering chains where the magnetic forces $f_{\rm push}$ have the numerical coefficient $\xi = const$ (Equation 26). Using $\tau_{\rm pl} \propto w$, one finds from Equation (39) $a \propto \beta/w$. This gives $w \propto a^{-1}$ for relativistic plasmoids ($a > 1$). For non-relativistic plasmoids $a \approx \beta^2$ and one finds $w \propto a^{-1/2}$. In summary, substitution of $w \propto \beta/a$ into Equation (27) gives

$$\frac{dL}{d\ln a} \propto \begin{cases} a^{q/2}, & a < 1 \\ a^{q-1}, & a > 1 \end{cases} \qquad (41)$$

The expected range of $0 < q < 1$ (Section 3.1) then implies that most of the power is deposited into mildly relativistic plasmoids, $a \sim 1$. The PIC simulations show $q \approx 0$ for small plasmoids (which have $a \gg 1$); this implies that the power fraction given to high-a plasmoids decreases as a^{-1}.

Monster plasmoids with the maximum $w \sim h$ and $\tau_{\rm pl} \sim \tau_{\rm T}$ have the minimum a. In the drag-limited regime this minimum value is

$$a_{\rm min} \sim \begin{cases} (\tau_{\rm T}/\tau_\star)^{-1/2}, & \tau_{\rm T} < \tau_\star \\ (\tau_{\rm T}/\tau_\star)^{-2}, & \tau_{\rm T} > \tau_\star \end{cases} \qquad (42)$$

Note also that the above estimates assume $\tau_{\rm pl} \lesssim 1$. For optically thick plasmoids, the force balance $f_{\rm push} = f_{\rm drag}$ is different from Equation (39) and becomes

$$\beta\gamma^2 \approx \tau_\star, \qquad \tau_{\rm pl} > 1. \qquad (43)$$

The simplest model of saturated plasmoid motion with $\xi = const$ implies that $\tau_\star = \xi/\beta_{\rm rec} \lesssim 1$ is a fixed constant; then all optically thick plasmoids are moving with the same speed given by Equation (43). The actual value of ξ can vary. Sironi et al. (2016) find $\xi \propto \beta$, so ξ is reduced for non-relativistic plasmoids. In addition, ξ (and hence $\tau_\star$) can be noisy, and deviations from the force balance, $f_{\rm push} = f_{\rm drag}$, are expected. This will affect the statistics of the chain bulk motions, and direct PIC simulations should be used to measure in detail the distribution of plasmoid speeds in the presence of Compton drag.

4. RADIATED SPECTRUM

Plasmoids with the broad distribution of Lorentz factors discussed in Section 3 upscatter soft seed photons and form a Comptonized spectrum. This is the dominant hard X-ray component of the magnetic flare, and below

we examine it in some detail using a Monte-Carlo simulation. Then we discuss additional emission components associated with high-energy particles and annihilation of $e^{\pm}$ pairs.

4.1. Chain Comptonization

Let us consider a reconnection layer of a given optical depth τ_T. The optical depth is dominated by $e^{\pm}$ pairs; it may vary by a factor of a few around $\tau_T \sim 1$ depending on the compactness parameter of the flare as discussed in Section 2.3.

Scattering of photons will sample the velocity field in the reconnection layer. Let $z = 0$ be the midplane of the layer; the plasmoids of various sizes move along the $\pm x$ directions. The plasma temperature will have nothing to do with Comptonization. To emphasize this point, in the simulation we will intentionally take the cold-plasma limit $T_e = 0$ (more realistically, the cooled plasma relaxes to the Compton temperature $kT_C \sim 10$ keV, which weakly affects the results).

Our simplified Monte-Carlo simulation is set up as follows. We inject soft photons with energies E_s in the midplane of the reconnection layer and follow their propagation and (multiple) scattering until they reach the boundary $|z| = h$. The layer is approximated as an infinite slab filled with plasma of uniform density $n_{\pm}$. The parameter τ_T is defined as $\tau_T = n_{\pm}\sigma_T h$.

We follow the propagating photon with a small timestep $\Delta t \ll h/c$. At each step, the local plasma velocity is assumed to be a random variable. The photon can be scattered by plasmoids (region I) or by the plasma between the plasmoids (region II) which converges toward $z = 0$ with speed $v_{\rm rec}$. The two regions contain equal amounts of plasma (by definition of the thickness h of the reconnection layer).[2] Therefore, our Monte-Carlo simulation will assume that the average column densities of regions I and II are equal, i.e. the probabilities for scattering in regions I and II are equal as long as scattering occurs with Thomson cross section. The actual (Klein-Nishina) cross section in the simulation depends on the photon energy and the local plasma velocity. In region II, the velocity is fixed at $\mathbf{v}_{\rm rec} = (0, 0, -v_{\rm rec}{\rm sign}(z))$ with $v_{\rm rec} = 0.1c$. In region I, the plasmoid speed is drawn from the distribution discussed in Section 3. Then the scattering probability during timestep Δt is determined according to the Klein-Nishina cross section.

It is convenient to deal with the distribution of $a = \beta^2\gamma^2$ instead of speed β. In the chain, the value of a is drawn randomly with a probability distribution $dP = f(a)\, da$. Thus a single function $f(a)$ encapsulates the chain behavior in our simulation. It is found from the condition $dL_{\rm sc}/d\ln a = dL/d\ln a$, where $L_{\rm sc}$ is the power gained by photons through scattering and L is the power deposited in the chain, e.g. given by Equation (41).

Energy extracted from the chain in one scattering of a photon of energy E is $\Delta E \approx aE$, and the total extracted power is

$$L_{\rm sc} = \dot{N}_{\rm sc} \int f(a)\, \Delta E\, da, \qquad (44)$$

where $\dot{N}_{\rm sc}$ is the total scattering rate in the chain. This implies $dL_{\rm sc}/da \propto a\, f(a)$ and

$$f(a) \propto a^{-2} \frac{dL}{d\ln a} \propto \begin{cases} a^{\psi_1}, & a < 1 \\ a^{\psi_2}, & a > 1 \end{cases} \qquad (45)$$

This relation simply states that the power deposited in a plasmoid with a given a is radiated through scattering with this a. Accurate values of ψ_1 and ψ_2 should be taken from PIC simulations of radiative reconnection. The estimate in Equation (41) gives $\psi_1 = q/2 - 2$ and $\psi_2 = q - 3$. The exact value of $q \sim 0$ is not critical, and we will fix $q = 0$ (we also calculated models with $q = 1/2$, with similar results). The choice of $\psi_1 = -2$ and $\psi_2 = -3$ may not be accurate, in particular for ψ_1. However, the key feature of $f(a)$ — the break at $a \approx 1$ — should be robust, based on the PIC simulations and the estimates of Compton drag.

The constant of proportionality in Equation (45) is determined by the normalization of the distribution function $\int f(a)\, da = 1$. The distribution extends over the range,

$$a_{\min} < a < a_{\max}. \qquad (46)$$

The choice of $a_{\max} \sim \sigma$ weakly affects the results as long as $a_{\max} \gg 1$; we fix $a_{\max} = 100$. The value of $a_{\min}$ will be adjusted to give a desired Compton amplification factor A. The factor $A = \bar{E}_{\rm esc}/E_s$ is defined as the average net energy gain of a photon between its injection with energy E_s and escape with energy $E_{\rm esc}$; it is directly calculated in the Monte-Carlo simulation.[3] In our simulations, the photons are injected with energy E_s drawn from a Planckian distribution with temperature $kT_s = 10^{-3}m_ec^2$. The three parameters that control the shape of the emerging spectrum are T_s, τ_T, and A.

Figure 1 shows the results for $A = 10$ and a few values of $\tau_T = 0.7$, 1.5, and 3. According to Equation (20) these values correspond to $u \approx 1.7$, 8, and 31, and the range $1.7 < u < 31$ can correspond to $5 \times 10^2 < \ell_B < 10^4$ if $Y f_{\rm HE} \sim 10^{-2}$. One can see in the figure that in all three cases the emerging spectrum has a hard slope and a sharp cutoff around 100 keV. The cutoff position moves from ~ 200 keV to ~ 50 keV as the optical depth increases from 0.7 to 3, which corresponds to ℓ_B increasing by a factor of 20 (if $Y f_{\rm HE}$ is assumed to be the same in the three models).

The cutoff position — a fraction of $m_ec^2 = 511$ keV — is the result of three effects. (1) Most of the chain power is given to mildly relativistic plasmoids ($\gamma\beta \sim 1$) which dominate Comptonization. (2) Klein-Nishina effects (electron recoil in scattering) become strong at photon energies $E > 100$ keV, which reduces emission at these energies. (3) Pair plasma in flares near black holes never develops a large optical depth $\tau_T \gg 1$. The optical depth slowly grows with compactness ℓ_B, which does not exceed 10^4. This behavior of τ_T is similar to the known property of thermal $e^{\pm}$ plasma in annihilation balance (Svensson 1984; Stern et al. 1995).

Photon upscattering by the plasmoid chain in many respects resembles thermal Comptonization. In particu-

---

[2] Scattering at $|z| > h$ will be neglected in the simulation presented below, assuming that the pair density quickly decreases at $|z| > h$ (Section 2.3).

[3] The amplification factor A is determined by $a_{\min}$ and τ_T. This dependence is controlled by the shape of $f(a)$, in particular the choice of ψ_1 in Equation (45). In our default model, we find numerically that $A = 10$ corresponds to $a_{\min} \approx 0.7(\tau_T/1.5)^{-1.6}$.
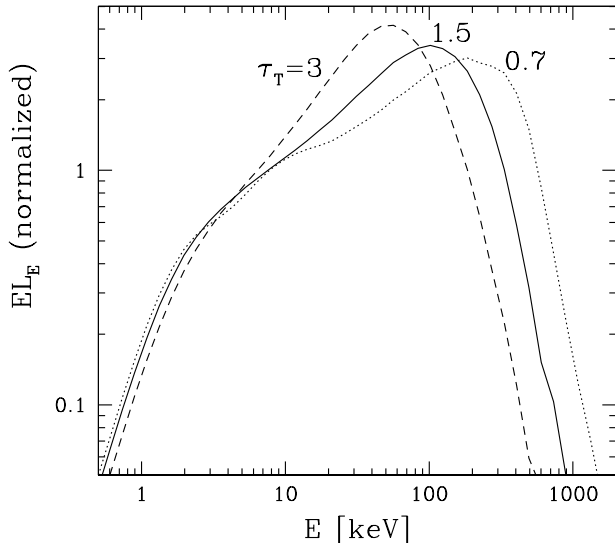
FIG. 2.— Spectrum emerging from the reconnection layer with Compton amplification factor $A = 10$. Three models are shown with optical depths $\tau_T = 0.7$, 1.5, and 3. The range of $0.7 < \tau_T < 3$ roughly corresponds to magnetic compactness varying by a factor of 20 around $\ell_B \sim m_p/m_e$. In all the models, the temperature of injected soft radiation is fixed at $kT_s = 10^{-3} m_e c^2$. Only the chain bulk Comptonization is simulated in the model. Additional emission from particles accelerated at the X-points will create a high-energy component that should emerge at $E \gtrsim m_e c^2$ and carry a few percent of the total energy budget (depending on f_{HE}); it is not shown in the figure and requires more advanced simulations.
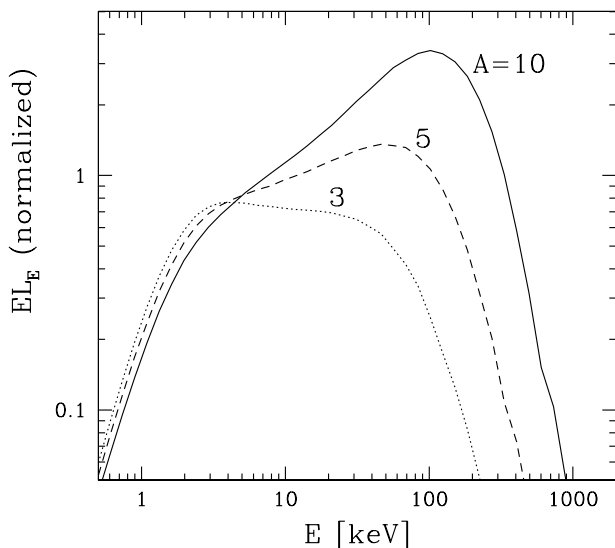

FIG. 3.— Spectrum emerging from the reconnection layer with Thomson optical depth $\tau_T = 1.5$ in three models with Compton amplification factors $A = 3$, 5, and 10.

lar, the flare spectrum depends on its Compton amplification factor A, which is controlled by how many soft photons are supplied to the reconnection region. The Comptonized spectrum becomes significantly softer if the

photon supply is increased by a factor ~ 3, so that the dissipated power per injected photon is reduced, giving $A = 3$ instead of 10 (Figure 3). This softening is expected, as a smaller A means that the probability for a scattered photon to reach high energies is reduced. Similar to standard thermal Comptonization, the relation between A and the spectral slope depends on T_s. The slope is softer for AGN, because their T_s is lower (see Beloborodov 1999a for a quantitive relation).

4.2. Nonthermal emission from young plasmoids

In addition to bulk Comptonization by the chain of cooled plasmoids, there is radiation from high-energy particles injected in young small plasmoids (Section 3.2). The characteristic Lorentz factor of these particles before their cooling is given by Equation (24); it is comparable to a few hundred. They generate synchrotron and high-energy IC emission with power L_{HE} that is a fraction f_{HE} of the total dissipated power,

$$L_{HE} = L_{syn} + L_{IC} = f_{HE} L. \qquad (47)$$

The transformation of the injected particle power L_{HE} into synchrotron and IC emission occurs in a few steps, because the IC photons with high energies $E_{IC} \lesssim \gamma_e m_e c^2$ do not escape and convert to secondary $e^\pm$ pairs outside the small plasmoids. The power of the $e^\pm$ cascade may compete with the synchrotron luminosity of the plasmoid itself, because its relativistic bulk motion reduces the synchrotron losses (Section 3.2).

The IC emission from the plasmoid is beamed along the chain direction (the x-axis) within the angle $\theta \sim \gamma^{-1}$. Therefore, the secondary pairs are injected with angles $\sim \theta$ with respect to the x-axis, which is also the direction of the background magnetic field. As a result, many secondary pairs are injected with modest pitch angles with respect to $\mathbf{B}$ and their synchrotron cooling is reduced by the factor of $\sin^2 \theta$. On the other hand, their IC cooling is reduced by a factor $\zeta_{KN} < 1$ due to the Klein-Nishina reduction in the scattering cross section. The ratio of IC and synchrotron luminosities generated by the secondary pairs may be estimated as $U_{rad} \zeta_{KN}/U_B \sin^2 \theta$.

The high-energy IC photons generate a nonthermal cascade with a pair yield $Y \lesssim 0.1$, contributing to the pair loading of the reconnection layer (Section 2.3). In contrast, the synchrotron photons are soft, and contribute to the seed radiation for Comptonization in the chain. The characteristic energy of synchrotron photons emitted by the secondary $e^\pm$ pairs is given by

$$E_{syn} \sim 0.3 \gamma_e^2 \hbar \omega_B \sim 10 \, B_8 \sin \theta \left(\frac{\gamma_e}{100} \right)^2 \text{ keV}. \qquad (48)$$

Some of the pairs will be created inside large plasmoids, which occupy a significant volume in the reconnection layer. Their magnetic fields are far from the background pre-reconnection field, and the injected pairs will have large pitch angles $\theta \sim 1$. These pairs may give the highest E_{syn}. In any case, E_{syn} is unlikely to exceed 10 keV and may be much lower, especially taking into account that the secondary pairs likely have $\gamma_e < 100$.

For sufficiently low $\gamma_e < \gamma_{abs}$, synchrotron self-absorption suppresses synchrotron emission. The value of γ_{abs} can be estimated using the absorption coefficient

$\mu_{\rm abs}$ (Ginzburg & Syrovatskii 1964) evaluated at $E_{\rm syn}$,

$$\mu_{\rm abs} \sim 10^2 \, \frac{e}{B \sin \theta} \, \frac{1}{\gamma_e^4} \, \frac{dn_\pm}{d\gamma_e}, \qquad (49)$$

where the numerical factor was evaluated using $d\ln n_\pm/d\ln \gamma_e \sim -2$. The energy distribution of the cooling pairs is governed by the continuity equation in the energy space,

$$\dot{\gamma}_e \, \frac{dn_\pm}{d\gamma_e} = \dot{n}, \qquad \dot{\gamma}_e = \frac{4}{3} \, \frac{\sigma_{\rm T} U_{\rm eff}}{m_e c} \, \gamma_e^2. \qquad (50)$$

Here $\dot{\gamma}_e$ is the cooling rate with $U_{\rm eff} = \sin^2 \theta \, U_B + \zeta_{\rm KN} U_{\rm rad}$, and $\dot{n}$ is the injection rate of pairs with Lorentz factors above γ_e. The injection rate may be written as

$$z_s \dot{n} = Y(\gamma_e) \, \frac{f_{\rm HE} U_B v_{\rm rec}}{m_e c^2}, \qquad (51)$$

where $Y(\gamma_e) \sim 10^{-2} - 10^{-1}$ is the pair yield above γ_e, and z_s is the characteristic thickness of the layer where the secondary high-energy pairs are injected.

The condition for self-absorption is $\mu_{\rm abs} z_s / \sin \theta \sim 1$, where θ is the injection angle of the pairs (and their synchrotron photons) with respect to the magnetic field. This condition gives

$$\gamma_{\rm abs} \sim \left(\frac{10^2}{\sin^2 \theta} \, \frac{e}{\sigma_{\rm T} B} \, Y f_{\rm HE} \, \beta_{\rm rec} \, \frac{U_B}{U_{\rm eff}} \right)^{1/6}$$
$$\sim \frac{15}{\sin^{1/3} \theta} \left(\frac{f_{\rm HE}}{0.1} \right)^{1/6} \left(\frac{M}{10 M_\odot} \right)^{1/12}, \qquad (52)$$

where we substituted B from Equation (9). Self-absorption is particularly strong in magnetic flares in AGN, which have a typical black hole mass $M \sim 10^8 M_\odot$.

Secondary particles with $\gamma_e < \gamma_{\rm abs}$ are cooled only by Compton scattering. Besides blocking synchrotron cooling, self-absorption also provides means for thermalization of $e^\pm$ pairs (Ghisellini et al. 1998; Poutanen & Vurm 2009). In addition, at low energies, thermalization is assisted by Coulomb collisions. Detailed calculations of these processes show how the injection of high-energy particles leads to a Comptonized component extending to MeV energies (Poutanen & Vurm 2009). This component was not included in our simple Monte-Carlo simulation. It should become visible in the spectrum of a magnetic flare at $E \gtrsim m_e c^2$ (where the emission from the chain bulk Comptonization is strongly suppressed). It should, however, be cut off by $\gamma\gamma$ absorption at $E \gg 1$ MeV. Any significant emission well above 1 MeV must originate at a larger distance from the black hole, most likely in a relativistic jet.

4.3. Annihilation radiation

The ratio of annihilation luminosity $L_{\rm ann}$ to the total power L dissipated (and radiated) by the reconnection layer is given by

$$\frac{L_{\rm ann}}{L} \approx \frac{2 m_e c^2 \dot{n}_{\rm ann} h}{U_B v_{\rm rec}} \approx \frac{3 \, \tau_{\rm T}^2}{16 \, \beta_{\rm rec}^2 \ell_B} \sim 10^{-2}. \qquad (53)$$

$L_{\rm ann}$ is comparable to the luminosity L_1 in MeV photons that create $e^\pm$ pairs. In a flare with the typical $\ell_B \gtrsim 10^3$, the annihilation timescale is shorter than the residence time of particles in the reconnection layer (Section 2.3), so a large fraction of the created pairs annihilate, approaching the annihilation balance. Then the annihilation luminosity is related to the efficiency of pair creation and may be written as

$$\frac{L_{\rm ann}}{L} \approx Y f_{\rm HE}. \qquad (54)$$

The annihilation photons have energies close to 511 keV in the rest frame of the pair plasma. Their observed energies will be affected by gravitational and Doppler shifts. The reconnection layer has a size comparable to the Schwarzshild radius r_g, and the plasma in the layer has significant bulk speeds. A large fraction of pairs annihilate inside plasmoids with fast random motions. Note also that the entire flare region may have an interesting bulk speed controlled by the net flux of radiation away from the accretion disk (Beloborodov 1999c). The pair plasma is light and its inertia is small, so it tends to assume an equilibrium speed along the magnetic field lines. This speed is such that the local net radiation flux, measured in the plasma rest frame, is perpendicular to the local magnetic field.

5. DISCUSSION

5.1. Radiative reconnection

Reconnection in magnetic flares near luminous accreting black holes occurs in the radiative regime, i.e. most of the dissipated energy promptly converts to radiation. The plasma in the reconnection layer is still organized in the self-similar chain of plasmoids, however radiative effects change the plasma state in three ways. (1) Most of the plasma is cooled to a temperature comparable to the Compton temperature of the radiation field, $kT_{\rm C} \sim 10$ keV. (2) A large number of $e^\pm$ pairs are created in the reconnection layer and its scattering optical depth becomes comparable to unity. (3) The bulk motions of pair-loaded plasmoids are limited by Compton drag. Monster plasmoids, which contain most of the plasma, are moving with mildly relativistic speeds. Small plasmoids move with high Lorentz factors γ, which are inversely proportional to the size (and optical depth) of the plasmoid, up to the maximum $\gamma = \sigma^{1/2}$.

A key feature of the radiative reconnection layer is that the plasma energy is dominated by the bulk motions of macroscopic plasmoids rather than thermal motions of individual particles. A fraction of particles reach high energies in intermittent acceleration events, in particular near the X-points, however they are quickly cooled and buried in the growing plasmoids of sizes $w \gg r_g/\ell_B$. Mergers of cooled plasmoids are inefficient in pushing electrons to high energies. Instead, dissipation in the reconnection chain mainly occurs through magnetic stresses stirring plasmoids against Compton drag. The distribution of the dissipated power L over the plasmoid size w is roughly estimated as $dL/dw \approx const$ at $w \ll r_g$. It peaks at large w, i.e. most of the power is deposited into large (mildly relativistic) plasmoids rather than small ones with high Lorentz factors.

Note that the ion component is not cooled, and ions should form a broad energy distribution as observed in the PIC simulations without cooling. However, the $e^\pm$ loading of the flare reduces the energy budget of the ion

component by the factor $Z^{-1} = \tau_T^{ep}/\tau_T \lesssim \sigma^{-1}$.

A simplest flare model would assume that the magnetic energy advected into the reconnection layer is continually converted to heat. This is not happening — the PIC simulations show no sign of continually heated Maxwellian plasma. Instead, nonthermal particles are accelerated at the X-points and deposited into young small plasmoids, which grow and cool down. Effectively, a fraction f_{HE} of the released magnetic energy is impulsively injected in the form of high-energy particles. The value of f_{HE} may be measured in PIC simulations. Based on existing results (L. Sironi, private communication), $f_{HE} \sim 0.1$ appears to be a reasonable estimate. The remaining fraction $1 - f_{HE}$ is deposited into plasmoid bulk acceleration by magnetic stresses.

Thus, dissipation in magnetic flares occurs through two distinct modes: Compton drag on the chain and particle acceleration at X-points. This explains "hybrid Comptonization" observed in the hard-state of Cyg X-1. It was previously modeled using a phenomenological picture of thermal+nonthermal dissipation (Coppi 1999) or pure nonthermal dissipation accompanied by electron thermalization through synchrotron self-absorption (Poutanen & Vurm 2009; Poutanen & Veledina 2014). The latter model fits the data only with a relatively low magnetic field (and a large size of the source), which is energetically inconsistent with magnetic flares. This difficulty is resolved when plasma is not required to sustain $kT_e \approx 100$ keV, and instead the observed hard X-rays are generated by the chain Comptonization.

5.2. X-ray spectrum

Figure 2 suggests that radiative reconnection is a natural producer of hard X-ray spectra observed in X-ray binaries and AGN, with no need to assume a hot Maxwellian plasma. In agreement with observations, the chain Comptonization produces a hard X-ray spectrum with a sharp cutoff around 100 keV. The model calculated in Section 4.1 has the same number of parameters as thermal Comptonization (T_s, A, τ_T), and can be used to directly fit the observed spectra.

The spectral cutoff is located below $m_e c^2 = 511$ keV for the reasons discussed in Section 4.1. Its exact position depends on the optical depth of the reconnection layer τ_T (Figure 2), which is regulated by pair creation. The expected range of the flare compactness $3 \times 10^2 \lesssim \ell_B \lesssim 10^4$ approximately corresponds to $0.5 \lesssim \tau_T \lesssim 3$, which results in variations of the cutoff position between 200 and 40 keV. A similar range is observed in the hard states of accreting black holes in X-ray binaries, e.g. Cyg X-1 and GX 339-4, and AGN.

The Comptonized hard X-ray spectrum forms because the plasmoid chain is exposed to soft radiation with luminosity L_s, which can be much smaller than the flare power L. The spectral slope of chain emission is controlled by the Compton amplification factor $A = L/L_s$. L_s can be generated by the flare itself in two ways: (1) part of the flare radiation is intercepted by cold gas in the accretion disk and reprocessed into soft photons, and (2) soft synchrotron radiation is produced by the electrons accelerated in the reconnection layer. The observed spectral slope of Cyg X-1 (photon index $\Gamma \approx 1.6$) requires $A \sim 10$, consistent with a low $L_s \sim 0.1L$.

The efficiency of reprocessing depends on the geometry of the disk+corona configuration, the albedo of the disk surface ionized by the flare, and the anisotropy of the flare emission. The flaring $e^{\pm}$ plasma is preferentially ejected away from the disk, which makes the emission strongly anisotropic and reduces its reprocessing/reflection (Beloborodov 1999c; Malzac et al. 2001). Uncertainties in the corona configuration may eventually be resolved by observations. In particular, the iron K_α line in the reflected spectrum provides a useful tool to study the innermost region of the accretion disk (Fabian 2016). Flares must be accompanied by X-ray reverberation due to reflection, which has been observed in AGN on timescales comparable to r_g/c (Kara et al. 2016). Future observations with rich photon statistics on short timescales may clarify the role of reprocessing in photon supply to the reconnection regions.

In addition to chain Comptonization, magnetic flares generate high-energy particles, which receive a fraction f_{HE} of the released power. Their energy partially converts to soft synchrotron radiation and partially feeds an IC cascade, which must form a spectral tail extending to $\gtrsim 1$ MeV. The high-energy component needs more detailed calculations similar to those in Poutanen & Vurm (2009). It may explain the observed spectral tail sticking out at $E \gtrsim m_e c^2$ in Cyg X-1 (McConnell et al. 2002). The composite spectrum is a natural result of the hybrid Comptonization by the chain and accelerated particles, however, the spectrum at high energies may be further complicated by additional contributions from the jet (Zdziarski et al. 2016).

Sustaining the optical depth $\tau_T \sim 1$ through pair creation implies a significant rate of $e^{\pm}$ annihilation, which should produce a spectral feature around 511 keV. Its luminosity is comparable to 1% of the flare power (Section 4.3). The annihilation line may be hard to detect because it is shifted and broadened by the gravitational and Doppler effects. There is, however, some evidence for pair plasma near accreting black holes. A broad, variable annihilation feature was seen in the recent outburst of V404 Cyg (Siegert et al. 2016) and previously reported in a few other black-hole candidates (Goldwurm et al. 1992; Sunyaev et al. 1992). No annihilation feature has yet been identified in Cyg X-1. The detailed shape of the spectrum around 0.5 MeV is difficult to measure, because of the relatively low flux and a modest detector sensitivity in this energy band.

Magnetic flares with $10^3 < \ell_B < 10^4$ are expected to occur in the powerful, magnetically dominated corona of the accretion disk or at the jet base. In addition, the described picture of radiative reconnection should apply to a broader class of magnetic flares. Flares with $10 \ll \ell_B \ll 10^3$ are still radiative, however they create less $e^{\pm}$ plasma, so the region stays optically thin. Then the emission is expected to have a more extended nonthermal spectrum. This may occur in a weak corona associated with a soft spectral state, generating an extended tail in the radiation spectrum. Low-ℓ_B flares can also happen in relativistic jets at some distance from the black hole.

REFERENCES

Beloborodov, A. M. 1999a, in Astronomical Society of the Pacific Conference Series, Vol. 161, High Energy Processes in Accreting Black Holes, ed. J. Poutanen & R. Svensson, 295

Beloborodov, A. M. 1999b, MNRAS, 305, 181

—. 1999c, ApJ, 510, L123

Cerutti, B., Werner, G. R., Uzdensky, D. A., & Begelman, M. C. 2014, ApJ, 782, 104

Coppi, P. S. 1999, in Astronomical Society of the Pacific Conference Series, Vol. 161, High Energy Processes in Accreting Black Holes, ed. J. Poutanen & R. Svensson, 375

Fabian, A. C. 2016, Astronomische Nachrichten, 337, 375

Fabian, A. C., Lohfink, A., Kara, E., et al. 2015, MNRAS, 451, 4375

Galeev, A. A., Rosner, R., & Vaiana, G. S. 1979, ApJ, 229, 318

Ghisellini, G., Haardt, F., & Svensson, R. 1998, MNRAS, 297, 348

Gierliński, M., & Zdziarski, A. A. 2003, MNRAS, 343, L84

Ginzburg, V. L., & Syrovatskii, S. I. 1964, The Origin of Cosmic Rays

Goldwurm, A., Ballet, J., Cordier, B., et al. 1992, ApJ, 389, L79

Guilbert, P. W., Fabian, A. C., & Rees, M. J. 1983, MNRAS, 205, 593

Guo, F., Li, X., Li, H., et al. 2016, ApJ, 818, L9

Huang, Y.-M., & Bhattacharjee, A. 2012, Physical Review Letters, 109, 265002

Kagan, D., Nakar, E., & Piran, T. 2016, ApJ, 826, 221

Kara, E., Alston, W. N., Fabian, A. C., et al. 2016, MNRAS, 462, 511

Loureiro, N. F., Samtaney, R., Schekochihin, A. A., & Uzdensky, D. A. 2012, Physics of Plasmas, 19, 042303

Lyubarsky, Y. E. 2005, MNRAS, 358, 113

Malzac, J., Beloborodov, A. M., & Poutanen, J. 2001, MNRAS, 326, 417

McConnell, M. L., Zdziarski, A. A., Bennett, K., et al. 2002, ApJ, 572, 984

Melzani, M., Walder, R., Folini, D., Winisdoerffer, C., & Favre, J. M. 2014, A&A, 570, A112

Odell, S. L. 1981, ApJ, 243, L147

Parfrey, K., Beloborodov, A. M., & Hui, L. 2013, ApJ, 774, 92

Parfrey, K., Giannios, D., & Beloborodov, A. M. 2015, MNRAS, 446, L61

Petropoulou, M., Giannios, D., & Sironi, L. 2016, MNRAS, 462, 3325

Phinney, E. S. 1982, MNRAS, 198, 1109

Poutanen, J., & Veledina, A. 2014, Space Sci. Rev., 183, 61

Poutanen, J., & Vurm, I. 2009, ApJ, 690, L97

Romanova, M. M., Ustyugova, G. V., Koldoba, A. V., Chechetkin, V. M., & Lovelace, R. V. E. 1998, ApJ, 500, 703

Rybicki, G. B., & Lightman, A. P. 1979, Radiative processes in astrophysics

Siegert, T., Diehl, R., Greiner, J., et al. 2016, Nature, 531, 341

Sikora, M., Sol, H., Begelman, M. C., & Madejski, G. M. 1996, MNRAS, 280, 781

Sironi, L., Giannios, D., & Petropoulou, M. 2016, MNRAS, 462, 48

Sironi, L., & Spitkovsky, A. 2014, ApJ, 783, L21

Stern, B. E., Poutanen, J., Svensson, R., Sikora, M., & Begelman, M. C. 1995, ApJ, 449, L13

Sunyaev, R., Churazov, E., Gilfanov, M., et al. 1992, ApJ, 389, L75

Svensson, R. 1984, MNRAS, 209, 175

—. 1987, MNRAS, 227, 403

Tchekhovskoy, A., Narayan, R., & McKinney, J. C. 2011, MNRAS, 418, L79

Uzdensky, D. A., Loureiro, N. F., & Schekochihin, A. A. 2010, Physical Review Letters, 105, 235002

Werner, G. R., Uzdensky, D. A., Cerutti, B., Nalewajko, K., & Begelman, M. C. 2016, ApJ, 816, L8

Zdziarski, A. A., & Gierliński, M. 2004, Progress of Theoretical Physics Supplement, 155, 99

Zdziarski, A. A., Malyshev, D., Chernyakova, M., & Pooley, G. G. 2016, ArXiv e-prints, arXiv:1607.05059